AIAA JOURNAL
Vol. 41, No. 5, May 2003

Axisymmetric Swirling Vortical Wakes Modulated by a Control Disk

R. F. Huang* and S. C. Yen†
National Taiwan University of Science and Technology, Taipei 10672, Taiwan, Republic of China

The effects of an above-exit circular disk on the flow structures, turbulence properties, and mixing characteristics of swirling jets separated by a large diameter blockage disk at jet exit are studied by using the smoke-wire flow-visualization technique and a two-component laser Doppler velocimeter. A carbon-dioxide tracer-gas experiment is conducted to examine the mixing capability of the flows modulated by the control disk. The smoke-streak flow patterns, characteristic lengths, velocity vectors, streamlines, velocity distributions, turbulence properties, and concentration distributions of the carbon dioxide are presented and discussed. Topological techniques are applied to analyze and interpret the flow patterns. With the variation of the distance between the control and blockage disks and the central jet Reynolds number, the bubble structures in the near field display complex behaviors of extension, escape, and encapsulation. Under the influence of the control disk, the central jet deflects radially, merges with the swirling annular flow, then turns downstream to form a recirculation bubble in the control-disk wake. This arrangement creates significant momentum exchange and drastic turbulence fluctuations. The drastic increase of the turbulence fluctuations expedites mixing of the fluids issued from the central and annular jets, particularly in the bubble encapsulation and gap flow regimes.

Nomenclature

A_a = area at exit of swirling jet $[= \pi(D_o^2 - D^2)/4]$, 550 mm^2
A_c = area at exit of central jet $(= \pi d^2/4)$, 19.6 mm^2
B = blockage ratio at exit of jets $(= D^2/D_o^2)$, 0.563
C_{CO_2} = concentration of carbon dioxide, %
$C_{\mathrm{CO}_2,\mathrm{O}}$ = carbon-dioxide concentration of flows in natural regime, %
D = diameter of blockage disk, 30 mm
D_c = diameter of control disk, 14 mm
D_h = hydraulic diameter of annular swirling jet at exit $(= D_o - D)$, 10 mm
D_m = mean diameter for calculation of swirl number $[= (D + D_o)/2]$, 35 mm
D_o = outer diameter of annular swirling jet at exit, 40 mm
d = exit diameter of central jet, 5 mm
H = distance from blockage disk to control disk
Q_a = volumetric flow rate of annular swirling flow
Q_c = volumetric flow rate of central jet
Re_a = exit Reynolds number of annular swirling flow $(= u_a D_h/\upsilon)$
Re_c = exit Reynolds number of central jet $(= u_c d/\upsilon)$
r = radial coordinate, originated from center of blockage disk
S = swirl number

$$\left[= \int_{D/2}^{D_o/2} u w r^2 \,\mathrm{d}r \Bigg/ \frac{D_m}{2} \int_{D/2}^{D_o/2} u^2 r \,\mathrm{d}r \right]$$

u = axial velocity component
u_a = volumetric mean axial velocity of annular swirling jet at exit $(= Q_a/A_a)$
u_c = volumetric mean velocity of central jet at exit $(= Q_c/A_c)$
v = radial velocity component
w = azimuthal velocity component
X = recirculation length of outer vortex, measured from blockage disk to maximum axial height of the outer recirculation bubble
x = axial coordinate, originated from center of blockage disk
η = mixing efficiency $[= (C_{\mathrm{CO}_2,\mathrm{O}} - C_{\mathrm{CO}_2})/C_{\mathrm{CO}_2,\mathrm{O}}]$
υ = kinematic viscosity of air or carbon dioxide

Introduction

THE swirling jets are widely employed in the industrial applications to benefit from the reverse flows in the near field, which can cause expedition of the mixing process. Imparting a swirl motion to a jet can cause a recirculation zone to form near the exit of the jet if the swirl and Reynolds numbers are beyond some critical values.[1-3] If a swirling jet has a large central blockage at the exit, the flow structure behind the central blockage will become complicated. Escudier and Keller[4] studied a swirling flow in a cylindrical tube with large cylindrical center bodies of blockage ratios 0.25 and 0.39. A recirculation bubble immediately behind the cylindrical centerbody and an isolated axisymmetric recirculation zone (i.e., vortex breakdown[5,6]) on the symmetry axis in the downstream section of the outer confining tube were observed. Sheen et al.[7] studied the structures of the recirculation zones of the swirling flows in a cylindrical tube with a centerbody of blockage ratio 0.23. Several complex characteristic flow modes were identified at different swirl strengths. Huang and Tsai[8] conducted a systematic search for the characteristic flow patterns behind the central blockage disks with a wide range of blockage ratio from 0.026 to 0.563. They found out that the bluff-body effect became significant when the blockage ratio was greater than about 0.11. For blockage ratios smaller than about 0.11, the conventionally measured recirculation bubble existing at the exit of the swirling jet is the vortex breakdown or the time-averaged streamline pattern of the dynamic instantaneous behavior of vortex shedding.[9] In the blockage-effect regime complex flow structures, which are called swirling vortical wakes, can be formed in the near field even at low swirl and Reynolds numbers. The flow structures such as the single bubble, dual rings, dual rings with vortex breakdown, and vortex shedding can exist in different regimes of swirl number and blockage ratio.[8]

In many industrial applications fluids have to be injected to the swirling vortical wake, which is induced by an annular swirling jet through a hole located at the center of the blockage disk installed at

---

Received 16 May 2002; revision received 8 November 2002; accepted for publication 13 November 2002.

*Professor, Department of Mechanical Engineering, 43 Keelung Road, Section 4; rfhuang@mail.ntust.edu.tw. Senior Member AIAA.

†Graduate Student, Department of Mechanical Engineering.

the exit of the jet, for example, nonpremixed bluff-body combustors, cooling systems, fluid mixers, industrial burners, propulsion apparatus, etc. Industrial apparatus using the swirling vortical wake can operate at low swirl and Reynolds numbers while still containing recirculation zones. Such flows were studied by investigators[10,11] because of their wide industrial applications and the significance in mixing and combustion processes. One of the features of the swirling vortical wake that is different from the nonswirling bluff-body wake is that there usually exists a flow rotating around the central axis and propagating downstream.[8] If a jet is injected into the swirling vortical wake through a central hole, the central jet fluids are brought directly to the downstream area by the central jet-like swirling flow.[9] This phenomenon causes a high density of the injected central jet fluid to concentrate around the central core region.[9] Alternately, injection through the circumferentially distributed holes in order to increase the resident time of fluids remaining in the swirling vortical wake was examined.[9] Only a slight improvement was found. Apparently, an alternative method must be sought to achieve the goal of mixing enhancement via modulation of the flowfield.

In this paper a control method is developed to circumvent the injection-through problem of the high-speed central jet by modulating the flow structures of the swirling vortical wake via a circular disk, which is placed at various distances from the blockage disk at the exit of an annular swirling jet. Effects of the above-exit control disk on the flows were examined by documenting the characteristic flow structures, turbulence properties, and tracer-gas concentration distributions. Because the jet Reynolds numbers employed in this study are low, the mixing mechanism induced by the drastically increased turbulent fluctuations might not be applied in the situations of high Reynolds numbers. However, the large-scale vortex behaviors and their effects on the mixing capability can still be applied in the practical mixing systems.

Experiments

The experiments were conducted in a test rig, as shown in Fig. 1. The swirling annular jet was supplied with a ring blower. The airflows driven from the ring blower went sequentially through the acoustical filters, pressure regulators, needle valves, rotameters, and fluidized-bed particle generators, then were fed into a cylindrical test rig, which is similar to the one illustrated by Huang and Tsai.[8] The azimuthal velocity component was imparted to the flow by an axisymmetric array of 12 guide vanes arranged on a pitch circle of radius 175 mm. The vane angles θ could vary from 0 to 70 deg with a resolution of 0.5 deg. A well-contoured nozzle with a contraction ratio 9.0 was used to accelerate the flow. A cylindrical test section with a diameter $D_o = 40$ mm was attached to the exit of the nozzle. A circular disk made of stainless steel with a diameter $D = 30$ mm and thickness of 1 mm was placed concentrically at the exit of the cylindrical test section to separate the central and annular jets. The blockage ratio was 0.563. Axial and radial coordinates x and r, respectively, were originated at the center of the circular disk in the exit plane, as defined in the subset of Fig. 1. Another circular disk made of stainless steel with a diameter $D_c = 14$ mm and thickness of 0.9 mm was placed horizontally at a distance H above the blockage disk. The distance H could vary from 3.0D to zero by adjusting the length of two small-diameter stainless-steel rods that fix the control disk at rims. The fixing rods had a diameter of 0.45 mm. The central jet fluids were provided from either a ring blower for flow measurement or from a CO_2 pressure tank for tracer-gas experiment. The air or the carbon-dioxide gas was fed into a nozzle assembly, in which large turbulence fluctuations were filtered by five layers of mesh screens. A seamless stainless-steel tube with a length of 600 mm and an inner diameter of 5.0 mm was adapted to the exit of the nozzle. Jet fluids were vented to the wake of the blockage disk via a 5.0-mm-diam hole located at the center of the disk.

The flow visualization was performed with a corrugated tungsten wire that was placed on the symmetry plane across the jet exit at $x/D_o = 0.025$. The wire had a diameter of 200 μm. Slight corrugations were made on the wire in order to control the thickness and spacing of the smoke streaks. Thin mineral oil was brush coated on the wire surface and electrically heated to generate fine smoke streaks. The Reynolds number based on the smoke-wire diameter

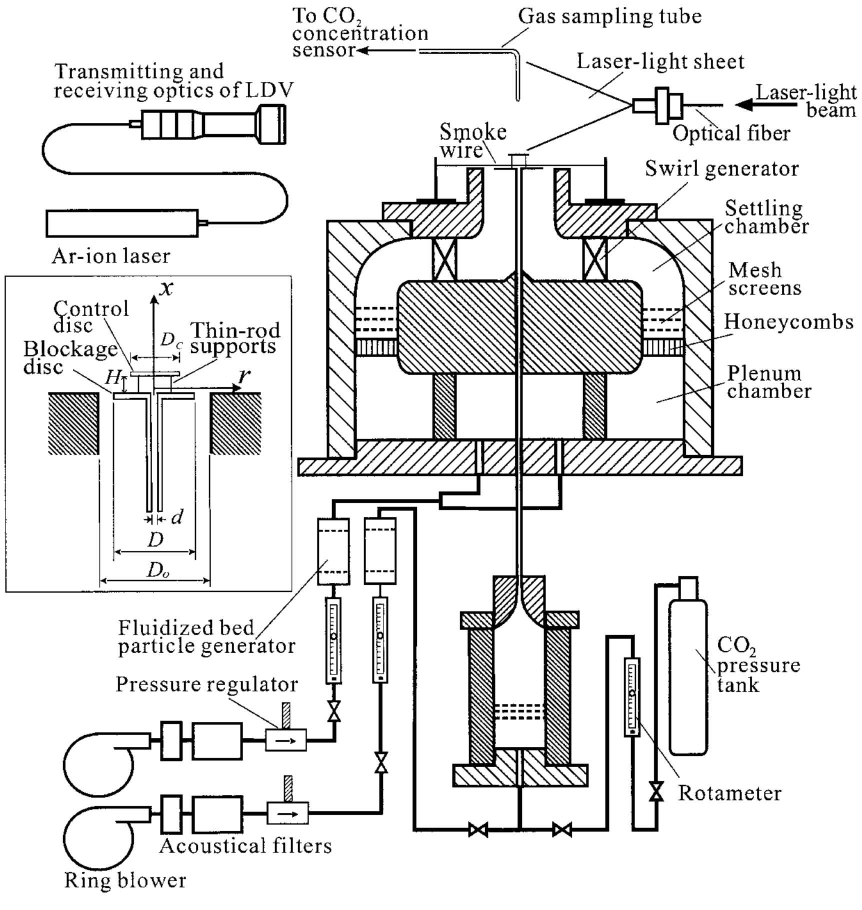

Fig. 1 Experimental setup.

was kept below 40 to avoid vortex shedding behind the wire.[12] The diameter of the aerosols of the condensed oil vapor measured by a Malvern 1600C Laser Particle Analyzer was 1.7 ± 0.3 μm. The Stokes number[13] of the oil aerosols was about the order of 10^{-3}, which is much smaller than unity. Therefore, the smoke streaks were expected to be able to follow the flow appropriately. The smoke streaks were illuminated by a 0.6-mm-thick laser light sheet on the symmetry plane. Two-dimensional streak images of the flow patterns were recorded on the computer at a rate of 30 fps through a charge-coupled device (CCD) camera accompanied with a high-quality image grabber.

The velocity field was measured with a two-component laser Doppler velocimeter (LDV). The blue and green laser beams supplied by a Spectra-Physics' Stabilite-2017 6-W argon-ion laser were separated and focused through the Dantec Fiber-Flow optical system. The dimensions of the measuring volumes of the green and blue components estimated at e^{-2} light intensity level were about $0.120 \times 0.120 \times 1.543$ and $0.114 \times 0.114 \times 1.463$ mm, respectively. The fringe separations of these components were 3.31 and 3.14 μm, respectively. The system was configured to operate in the backscatter mode. A Bragg cell was embedded in the system to distinguish the directional ambiguity. A Dantec FVA Enhanced two-component correlation processor was used to convert the Doppler signals into frequency data. The frequency data were fed into a PC-controlled data acquisition system to calculate the average velocities and other statistical properties. Each velocity data record consisted of 10,000 samples, which would last for about 1.3 s. The average sampling rate was about 7.7 kHz. A series of tedious preexperimental tests showed that the measured average velocities and turbulence properties approached stable when the number of samples was greater than 6000 and the elapse time was longer than 0.8 s. The 7.7-kHz sampling rate could resolve at least about 3.9-kHz fluctuations in the flow. Magnesium-oxide particles with an average diameter of 5 μm were seeded into both the central and annular flows via two fluidized-bed particle generators to scatter the laser light. The seeding particles could respond up to 3.6 kHz according to Mei.[14]

The axial and tangential exit velocity profiles of the annular swirl flows and central jet at various swirl numbers were measured across $x/D = 0.07$ plane with the two-component LDV. Radial distributions of the peak-value-normalized velocity components at the exit of the swirling annular flow showed profile similarities in wide band of swirl numbers. The normalized axial velocity profiles displayed an increase from the edge of the disk to attain a maximum at $r/D \approx 0.56$, then declined outward. The similarity profiles of the azimuthal velocities peaked at $r/D \approx 0.6$. The exit velocity profile of the central jet was almost parabolic. In the range of this study, the axial and tangential turbulence intensities at the exit of the annular flow, which were measured by LDV, were lower than 3.6 and 2.7%, respectively. The axial turbulence intensities at the exit of the central jet were lower than 0.8%.

The swirl intensity of a swirling flow is characterized by the swirl number S, which is defined by

$$S = \left[\int_{D/2}^{D_o/2} u w r^2 \, \mathrm{d}r \middle/ \frac{D_m}{2} \int_{D/2}^{D_o/2} u^2 r \, \mathrm{d}r \right]$$

(Refs. 1 and 10). It is a ratio of the axial flux of angular momentum to the axial flux of axial momentum. The exit swirl numbers in this study are obtained by applying the exit axial and tangential velocity components u and w to the preceding definition of swirl number.

The local carbon-dioxide concentration was measured with a Rosemount Model 880A carbon-dioxide gas analyzer. The probe used for gas sampling was a stainless-steel tube with a diameter of 2 mm. The gases were continuously drawn through the probe and a dehumidifying system, which contained a suction pump, then directed into the gas analyzer. Throughout this experiment the gas suction rate was kept as low as possible for measurement sensitivity of the gas analyzer in order to ensure a near-isokinetic situation that the probing and suction would cause minimum influences on the flow. This was done by constantly monitoring the smoke-wire flow images via the CCD camera. The output data of the gas analyzer were fed to a data acquisition system to calculate average values. Each data record consisted of 32,000 samples and lasted for 21 s.

The rotameters that were used to measure the flow rate of the air jet and carbon-dioxide gas were calibrated in the laboratory with a microflow calibration system. The maximum uncertainty was ±2% of reading at low flow rates. The low uncertainty of the laboratory-calibrated rotameters ensures the accurate and steady supplies of the air and carbon dioxide. The accuracy of the velocity measurements depends on many complex factors, for example, optical noise, electronic noise, filtering bandwidth, gain setting, fringe-pattern distortion, beam-waist adjustment, etc. It is much easier to sum them up and estimate by comparing the measured velocities of a rotating fine wire with the tangential velocity of the rotating wire at the measurement point. The results show that the uncertainty of the mean velocity measurements was less than ±1.8% of reading. The standard deviation of the random errors is approximately within ±2.1% of center value. The estimated uncertainties of the turbulence intensities and Reynolds stresses are less than ±3.9%. The uncertainty of the CO_2 concentration measurement by using the Rosemount Model 880A carbon-dioxide gas analyzer was 0.25% at the reading of 80%, 0.3% at the reading of 30%, and 0.8% at the reading of 1%, according to the calibration curve.

Results and Discussion

Smoke-Streak Flow Patterns and Characteristic Flow Regimes

Figure 2 shows the control-disk-modulated smoke-streak flow patterns of the swirling vortical wakes at $Re_a = 2.18 \times 10^2$ and $S = 0.194$. The exposure time is 0.01 s. Because the average annular velocity at the jet exit and the disk diameter were 33 cm/s and 3 cm, respectively, the typical timescale of the large vertical flow structures in the flowfield is estimated to be about 0.1 s. A 0.01-s exposure time taken for the pictures of Fig. 2 is short enough to freeze the images of the large-scale flow motions. The smoke streaks show

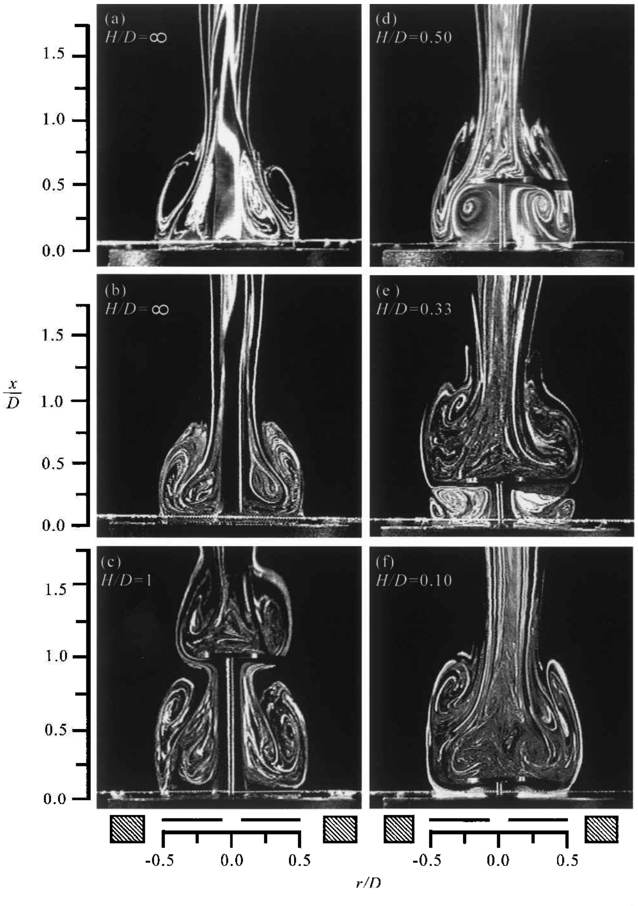

Fig. 2 Pictures of smoke-streak flow patterns. $Re_a = 2.18 \times 10^2$ ($S = 0.194$): a) and d) $Re_c = 1.50 \times 10^2$ and b), c), e), and f) $Re_c = 3.66 \times 10^2$; shutter speed = 0.01 s.

a little asymmetric flow patterns because of the characteristics of the instantaneous vortical flows. Depending on the distance H between the blockage and control disks, several types of flow patterns are observed.

Figures 2a and 2b show the natural flows (i.e., no control disk is applied, denoted by $H/D = \infty$) at $Re_c = 1.5 \times 10^2$ and 3.66×10^2, respectively. The axial momentum ratios of the central to annular flows at exit are 0.69 and 1.68, respectively. A dual-ring flow structure, which has been discussed by Huang and Tsai,[8] appears in the near-wake region. The outer and inner vortex rings as well as a central swirling jet-like flow are highly distinguishable in the smoke-streak pattern. At $Re_c = 1.5 \times 10^2$ the central jet fluids are "absorbed" into the vortex rings, whereas at $Re_c = 3.66 \times 10^2$, the central jet fluids shoot directly downstream along with the central swirling jet-like flow.

When the control disk is installed at $H/D = 1$ with $Re_c = 3.66 \times 10^2$, as shown in Fig. 2c, the axial bubble length is extended. The central jet impinges to the upstream surface of the control disk, diverts radially outward along the disk, shoots a short distance away from the disk rim as a result of the inertial of the jet fluids, turns upward, and forms a vortical wake downstream of the control disk. When the control disk is installed at $H/D = 0.5$ with $Re_c = 1.5 \times 10^2$, the outer vortex ring escapes from the edge of the control disk, as shown in Fig. 2d. The inner vortex ring remains in the space between the control and blockage disks. When the control disk is installed at $H/D = 0.33$ with $Re_c = 3.66 \times 10^2$, as shown in Fig. 2e, both the outer and inner vortex rings are encapsulated within the space between the control and blockage disks. The inner vortex ring occupies a large space between the disks so that the relative positions and sizes of the inner and outer vortex rings become dramatically different from those of Fig. 2c. The vortical wake downstream of the control disk enlarges drastically. When the control disk is installed very close to the blockage disk at $H/D = 0.1$ with $Re_c = 3.66 \times 10^2$, as shown in Fig. 2f, no vortical flow structure is found in the gap between the disks. The dual-ring flow pattern, which looks similar to Fig. 2b of the natural state, appears. However, the bubble size becomes much larger.

Figure 3a shows the variation of the normalized axial length of the outer vortex ring with the normalized axial height of the control disk. The axial length of the outer vortex ring was measured from the blockage disk to the maximum height of the outer recirculation bubble by averaging 30 smoke-streak flow images. In doing such measurements, the images were magnified 10 times to reduce the measurement error. Uncertainties of the characteristic length data measured from the smoke-streak photographs were estimated to be less than 5% of the blockage disk diameter. For H/D greater than about 1.4, the control disk has no effect on the swirling vortex rings. A term "natural regime" is used for flows at this state. The bubble length at $Re_c = 1.5 \times 10^2$ is larger than that at $Re_c = 0$ because the central jet momentum is not large enough to penetrate the bubble. Therefore the central jet fluids are distributed into the bubble itself. At $Re_c = 4.5 \times 10^2$ the central jet penetrates through the bubble, and the high shear induced by the high-speed central jet brings away bubble fluids, increases vorticities, and causes low local pressure. The bubble hence shortens. These phenomena are similar to those observed by Huang and Lin[15] for the case of nonswirling double concentric jets. When H/D is smaller than about 1.4 and greater than about 0.83, the bubble lengths at all central jet Reynolds numbers increase with the decrease of H/D. A term bubble extension is employed for flows in this regime. When H/D is between about 0.83 and 0.12, the bubble lengths at $Re_c = 0$ and 1.5×10^2 increase with the decrease of H/D because the outer vortex ring escapes from the control disk rim. At $Re_c = 4.5 \times 10^2$ the outer vortex ring shortens with the decrease of H/D because the dual rings are encapsulated and compressed by the control disk. When H/D is smaller than about 0.12, which is in the gap flow regime, the bubble lengths increase at $Re_c = 0$ and 1.5×10^2.

The characteristic flow patterns shown in Fig. 2 are typical. They can be identified in the parameter domain of the normalized height of control disk H/D and the central jet Reynolds number Re_c, as shown in Fig. 3b. Identification of the flow regimes is based on the smoke-streak flow patterns and the axial length variations of the swirling vortical bubble. The boundaries that separate different characteristic flow regimes bear some uncertainties. Maximum ambiguity in identifying the boundaries between different flow regimes is about ±0.05 for H/D and about ±10 for Re_c.

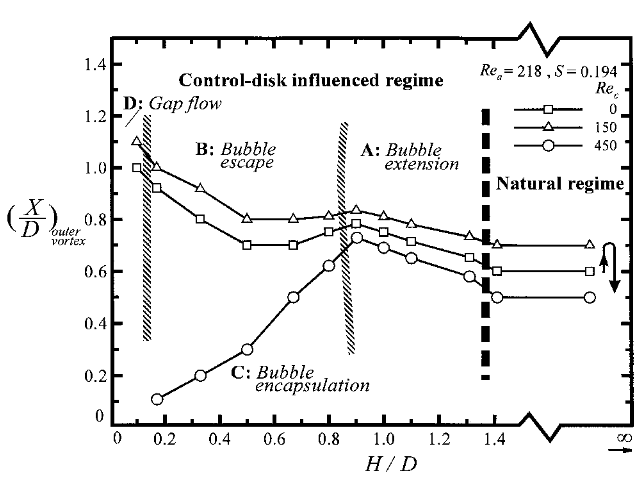

Fig. 3a Normalized axial length of outer vortex ring at various of Re_c.

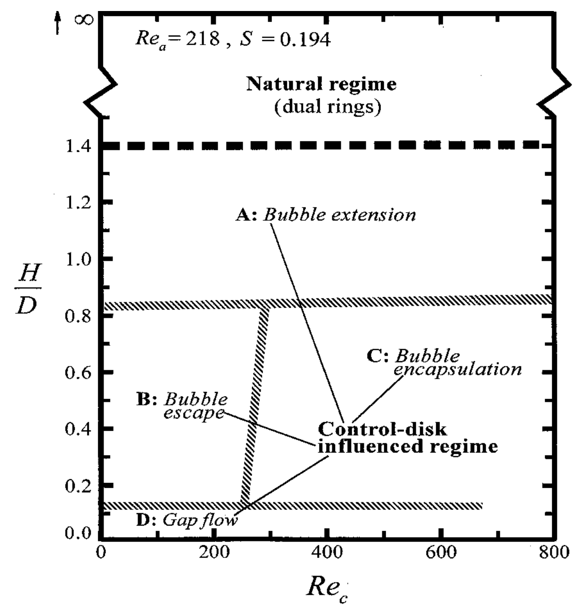

Fig. 3b Characteristic flow regimes: $Re_a = 2.18 \times 10^2$ and $S = 0.194$.

Velocity Vectors and Streamlines

Figures 4–6 show the LDV-measured velocity vectors and streamline patterns of the flows under different controlled states. The streamlines are obtained by using the shooting method.

As shown in Fig. 4a for flows in the natural regime, a pair of counter-rotating vortex rings with two nodes at $x/D \approx 0.19$ and 0.53 is formed in the near wake. The flows along the central axis go all of the way downstream so that no stagnation point is found on the central axis. An off-axis saddle point exists at $(x/D, r/D) \approx (0.82, 0.16)$. In Fig. 4b for flows in the bubble extension regime, the flow pattern near the upstream surface of the control disk alters. The central jet is deflected by the control disk, goes in the radial direction, merges with the annular swirling flow, and then turns upward around the disk rim. This new boundary condition would induce an up-shear effect on the upstream flows and stretch the swirling vortical bubble. Consequently, the normalized height of the outer vortex ring increases to $x/D \approx 0.92$. (The data are 0.85 in Fig. 4a.) To adapt the radially diverted jet, the off-axis saddle point moves upstream to $x/D \approx 0.74$. (The data are 0.82 in Fig. 4a.) Downstream of the control disk, a single-ring, close-top toroidal bubble is formed because there exists a stagnation point on the central axis.

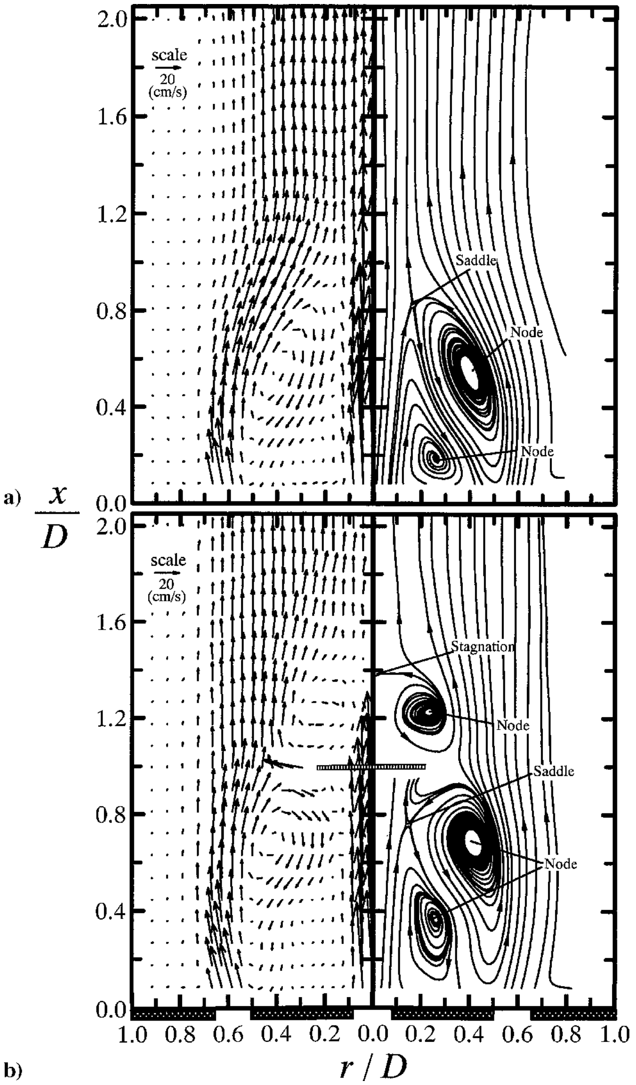

Fig. 4 Velocity vector field (left) and streamline pattern (right) of flows in a) natural regime $H/D = \infty$ and b) bubble extension regime $H/D = 1.0$: $Re_a = 2.18 \times 10^2$ ($S = 0.194$) and $Re_c = 3.66 \times 10^2$.

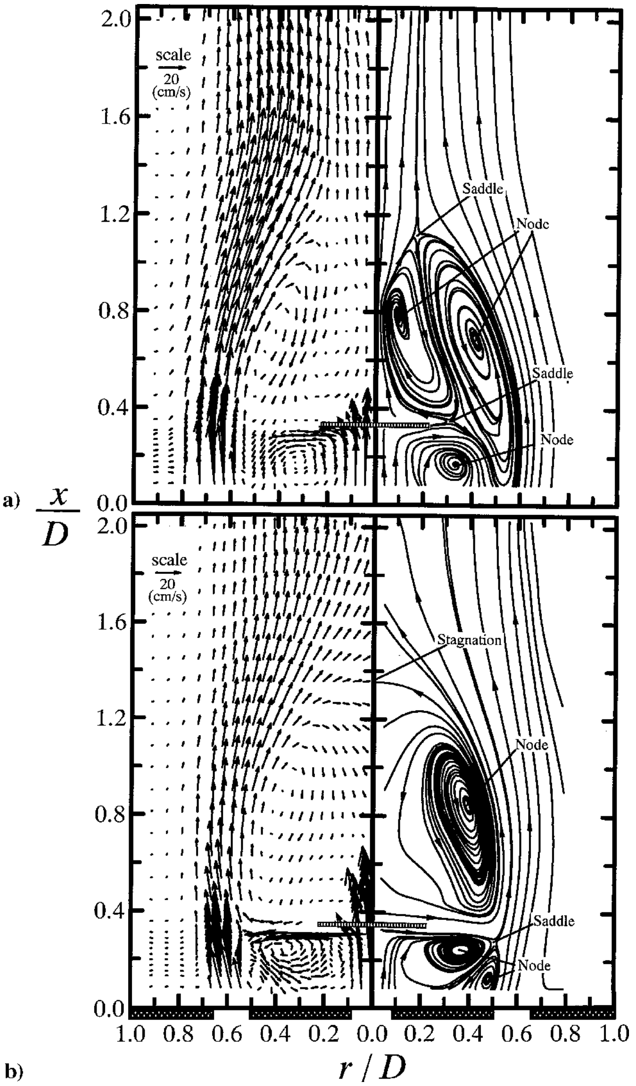

Fig. 5 Velocity vector field (left) and streamline pattern (right) of flows in a) bubble escape regime $H/D = 0.33$, $Re_c = 1.50 \times 10^2$ and b) bubble encapsulation regime $H/D = 0.33$: $Re_c = 3.66 \times 10^2$ and $Re_a = 2.18 \times 10^2$ ($S = 0.194$).

Figure 5a shows the flows in the bubble escape regime. The outer vortex ring elongates across the control disk to form a four-way saddle at the height of $x/D \approx 1.12$, which is far above the control-disk height $x/D = 0.33$. The inner vortex ring still exists between the control and blockage disks. Because the central jet Reynolds number is not high, the deflected flows do not overshoot radially far away from the control disk rim before they turn upward. The off-axis four-way saddle moves up to $(x/D, r/D) \approx (0.35, 0.30)$, which is near the control disk rim. Figure 5b shows the flows in the bubble encapsulation regime at $H/D = 0.33$. Large radial velocity vectors are induced by the deflected central jet and overshoot radially far away from the control disk rim. This disk-diverted stream stretches the inner vortex in the radial direction to $r/D \approx 0.5$ at the level $H/D = 0.26$, where a saddle point locates. The outer vortex ring is thus suppressed and located below the inner one. The single-ring close-top toroidal vortex situated on the control disk becomes much larger than that in the bubble extension regime because the blockage range of the control disk is virtually extended to $r/D \approx 0.5$ as a result of the radially diverted central flows. A stagnation point exists on the central axis at $x/D = 1.36$.

In Fig. 6 the jet issued from the central hole is deflected by the control disk, turns to the radial direction, and goes radially in the narrow space between the control and blockage disks. A dual-ring flow structure similar to that in the natural regime is found. The inner vortex ring is situated above the control disk, whereas the outer vortex ring is formed above the blockage disk. An off-axis saddle point is located at $x/D \approx 1.1$, which is much higher than 0.82 of Fig. 4a for its counterpart in the natural regime.

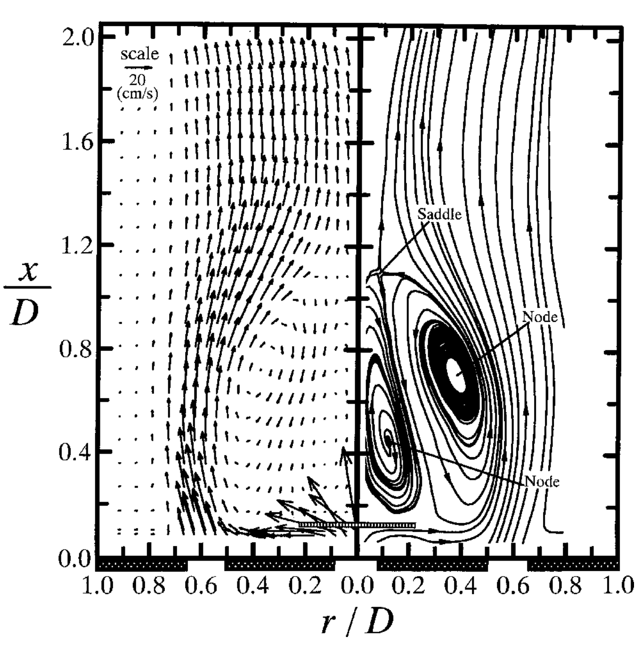

Fig. 6 Velocity vector field (left) and streamline pattern (right) of flows in gap flow regime at $H/D = 0.1$: $Re_a = 2.18 \times 10^2$ ($S = 0.194$) and $Re_c = 3.66 \times 10^2$.

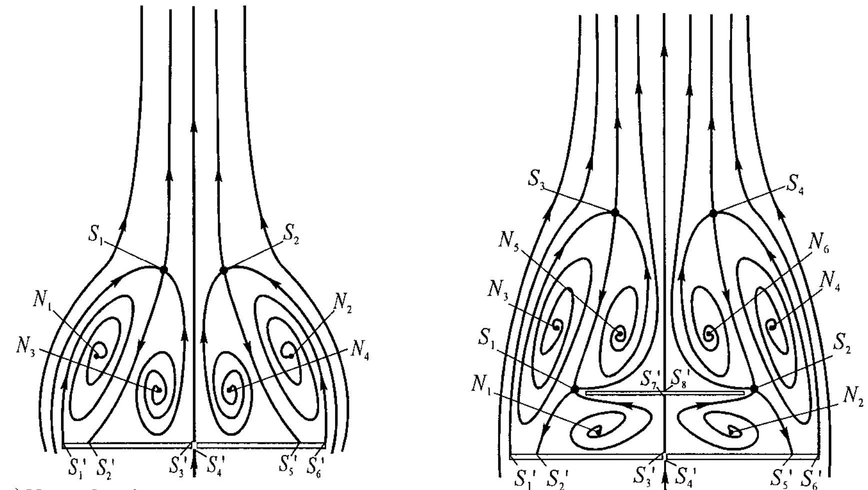

a) Natural regime

c) Bubble escape regime

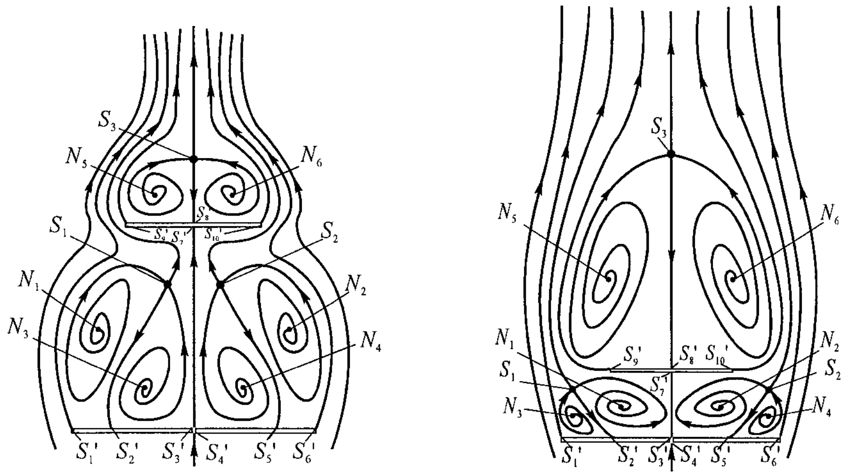

b) Bubble extension regime

d) Bubble encapsulation regime

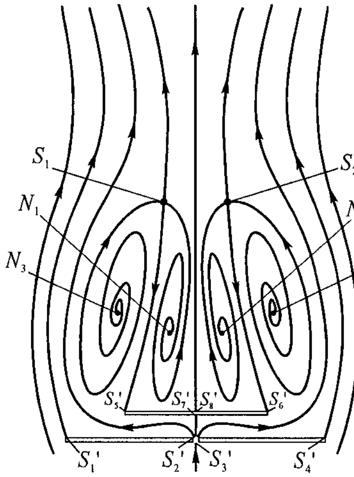

e) Gap flow regime

Fig. 7 Proposed topological flow structures.

Topological Analysis

Hand sketches of the topological flow structures are shown in Fig. 7. The topological sketches are obtained by employing the critical point theory, which was developed by Perry and Fairlie,[16] Chong and Perry,[17] and Lighthill.[18] With the critical point theory Perry and Steiner[19] have identified the sectional streamline patterns including nodes (foci or centers), saddles, bifurcation lines, and their combinations by depicting the separatrices, critical points, and alleyways. This technique can assist in revealing the features in the flowfield, either the steady flow structures or the evolution process of unsteady vortical motions.

In Fig. 7a several critical points appear on the proposed topological model: four nodes denoted by N_1–N_4, two off-axis four-way saddles denoted by S_1 and S_2, as well as six three-way saddles denoted by S_1'–S_6'. From the topological point of view, the flow reversal in the outer vortex ring causes the inner vortex ring to form, which in turn establishes the jet-like swirling flow along the central axis to expel the fluids to the downstream area. Hunt et al.[20] obtained a general formula for the relationship between the numbers of nodes (including four-way nodes N and three-way nodes N') and saddles (including four-way saddles S and three-way saddles S') for the flows around surface obstacles: $(\Sigma N + \frac{1}{2}\Sigma N') - (\Sigma S + \frac{1}{2}\Sigma S') = 1 - n$, in which n is the connectivity of the section of the flow under consideration. In the present case $n=2$ because an object is located in the flowfield. By counting the numbers of the critical points in Fig. 7a, that is, $\Sigma N=4$, $\Sigma N'=0$, $\Sigma S=2$, and $\Sigma S'=6$, the expression $(\Sigma N+\frac{1}{2}\Sigma N')-(\Sigma S+\frac{1}{2}\Sigma S')$ becomes -1, which satisfies the topological rule.

The topological flow models shown in Figs. 7b and 7d for the flows in the bubble extension and encapsulation regimes present the same numbers of the critical points: $\Sigma N=6$, $\Sigma N'=0$, $\Sigma S=3$, and $\Sigma S'=10$. In these cases $n=3$ because of the existence of the control disk. The topological rule is satisfied because $(\Sigma N+\frac{1}{2}\Sigma N')-(\Sigma S+\frac{1}{2}\Sigma S')=-2$. The primary differences among these two flow patterns are the relative positions and sizes of the inner and outer vortex rings and the size of the close-top toroidal recirculation bubble in the wake of the control disk. The combined effects induced by the strength of the central jet momentum and the height of the control disk cause the differences in the flow patterns.

Figure 7c shows the topological flow pattern of the flows in bubble escape regime. There is no stagnation point on the central axis above the control disk. Because of the existence of the four-way saddles S_1 and S_2, the control-disk rim no longer serves as three-way saddles. In this case $\Sigma N=6$, $\Sigma N'=0$, $\Sigma S=4$, and $\Sigma S'=8$, which satisfy the topological rule $(\Sigma N+\frac{1}{2}\Sigma N')-(\Sigma S+\frac{1}{2}\Sigma S')=1-n$, where $n=3$.

Although the dual-ring bubble structures in Figs. 4a and 6 look similar, the topological sketch shown in Fig. 7e is different from that in Fig. 7a. The numbers of the critical points of Fig. 7e are $\Sigma N=4$, $\Sigma N'=0$, $\Sigma S=2$, and $\Sigma S'=8$ for $n=3$.

Velocity Characteristics

Figure 8 shows the normalized axial-velocity distributions along the central axis when the control disk is placed at various heights. The vertical bars, which were filled with short slashed lines, indicate the axial locations of the control disk. At $H/D=\infty$ the axial velocities along the central axis are all positive because no stagnation point exists on the central axis as mentioned in Fig. 4a. The velocity profile decreases gradually from the jet exit to $x/D\approx 0.82$, where the off-axis saddle point is located, decreases steeply until $x/D\approx 1.2$, and then remains almost constant in the downstream area. The flow regimes, recirculation, transition, and established zones noted on the plot coincide with the characteristics of a typical turbulent jet flow. At $H/D=0.1$ the axial velocities along the central axis are also all positive. Although the streamline patterns of the dual-ring flow structures in the natural and gap flow regimes look similar, the velocity distributions are quite different. At $H/D=1.0$ and 0.33 the axial velocities along the central axis are negative within the recirculation bubble, which is located downstream of the control disk. Apparently, a lot of the axial momentum along the central axis downstream of the control disk in the disk-influenced regime is lost when compared to the flow in the natural regime.

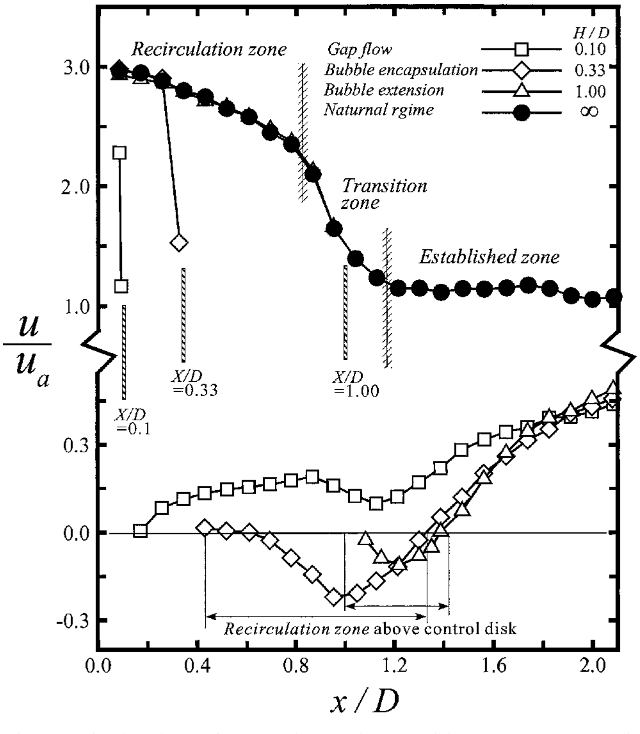

Fig. 8 Distributions of normalized axial velocities along central axis in various characteristic flow regimes: $Re_a=2.18\times 10^2$ ($S=0.194$) and $Re_c=3.66\times 10^2$.

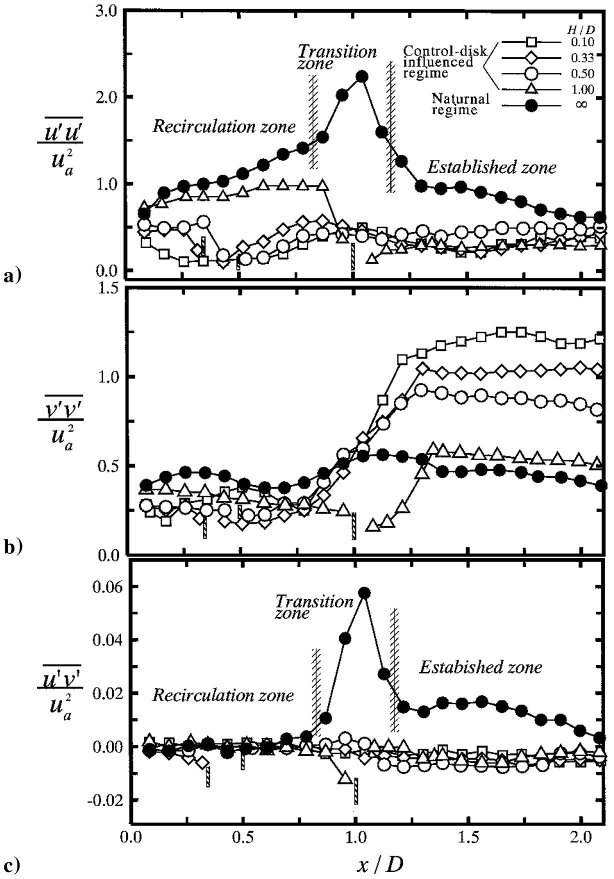

Fig. 9 Distributions of normalized turbulence properties along central axis in various characteristic flow regimes: $Re_a=2.18\times 10^2$ ($S=0.194$) and $Re_c=3.66\times 10^2$.

Figure 9 shows the turbulence properties along the central line at various H/D. At $H/D=\infty$ both the normalized axial normal stress $\overline{u'u'}/u_a^2$ and shear stress $\overline{u'v'}/u_a^2$ have very high values in the transition zone. They attain peak values at $x/D\approx 1.05$, which is located at the inversion point of the axial velocity profile shown in Fig. 8. The normalized axial normal stress $\overline{u'u'}/u_a^2$ and shear stress $\overline{u'v'}/u_a^2$ of the flows in the control-disk influenced regime are low when compared with the peak values of the natural flows, as shown in Figs. 9a and 9c. The normalized lateral normal stress $\overline{v'v'}/u_a^2$ of the disk-controlled flows increases with the axial extension of the recirculation bubble downstream the control disk, as shown in Fig. 9b. In the region just downstream of the control-disk bubble, the normalized lateral normal stress $\overline{v'v'}/u_a^2$ of the flows in the bubble encapsulation and gap flow regimes is significantly higher than that in the natural regime. These large lateral fluctuation intensities would possibly promote strong lateral momentum and mass exchange to the fluid in the wake.

The radial distributions of the velocity characteristics at $x/D=1.33$ reveal two features. First, the axial momentum in the wake region of the control-disk-influenced regime is apparently less than that in the natural regime, as shown in Fig. 10a, whereas the situation is reversed for the lateral momentums, as shown in Fig. 10b. Second, the radial distributions of the turbulent stresses in Fig. 10c show that the normalized axial normal stresses $\overline{u'u'}/u_a^2$ of the flows in the control-disk-influenced regime in the wake region of the control

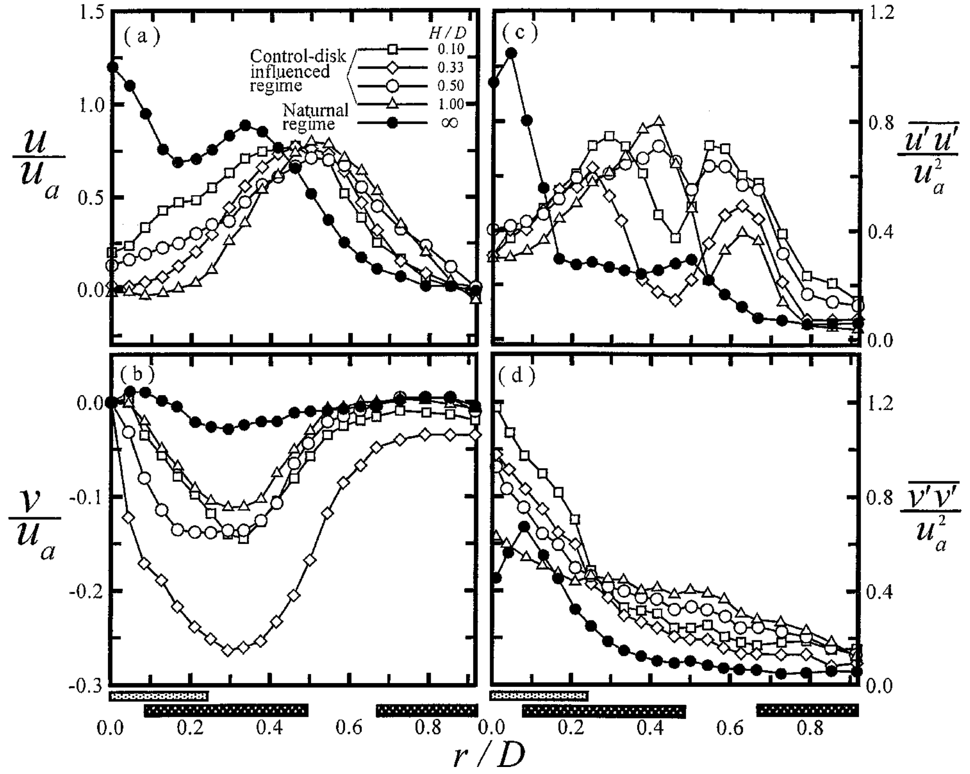

Fig. 10 Radial distributions of normalized axial and radial velocities (a, b) and turbulence properties (c, d, e) on the level $x/D = 1.33$: $Re_a = 2.18 \times 10^2$ ($S = 0.194$) and $Re_c = 3.66 \times 10^2$.

disk are larger than those in the natural regime excluding the area near the central axis. In Fig. 10d the values of lateral normal stresses $\overline{v'v'}/u_a^2$ in the control-disk-influenced regime are significantly larger than those in the natural regime.

Apparently, the central flows lose axial momentum as a result of the blockage of the control disk. The axial momentum of the central flows diverts radially, merges with the swirling annular flows, passes over the control disk, forms the recirculation bubble behind the control disk, then transfers a large amount of it to lateral momentum and strong turbulent fluctuations. This transformation of momentum induces a drastic increase of the lateral turbulent fluctuations in the whole wake region and a moderate increase of the axial fluctuations in the wake excluding the central core area. An increased mass diffusion between the central jet fluids and the annular swirling flows that are induced by the dramatic increases of the turbulent fluctuations would thus be expected, particularly in the bubble encapsulation and gap flow regimes.

Tracer-Gas Concentration Distributions

In the experiments of the tracer-gas concentration measurements, the air supplied to the central jet was replaced by the carbon-dioxide gas. Figure 11a shows the carbon-dioxide concentration measured at $x/D = 1.33$ on the central axis at various H/D. The carbon-dioxide concentration of the flow at the natural state decreases with the increase of the annulus Reynolds number. The regimes marked on the plot, such as the single bubble, dual rings, vortex breakdown, and triple ring, are characteristic flow modes presented by Huang and Tsai.[11] A drastic decrease of the carbon-dioxide concentration in the regime of vortex breakdown is natural because the mixing is expedited as a result of the formation of a recirculation bubble in the flowfield on the central axis. All of the carbon-dioxide concentration profiles of the flows in the control-disk-influenced regime are much lower than those in the natural regime.

To compare the efficiency of the mixing capability of the flows in the control-disk-influenced regime, a normalized difference of the carbon-dioxide concentration between the flows in the natural state and the control-disk-influenced regime is defined and denoted by η. According to the definition listed in the Nomenclature, the mixing efficiency η is the percentage decrease of the carbon-dioxide concentration of the control-disk-modulated flow from the corresponding

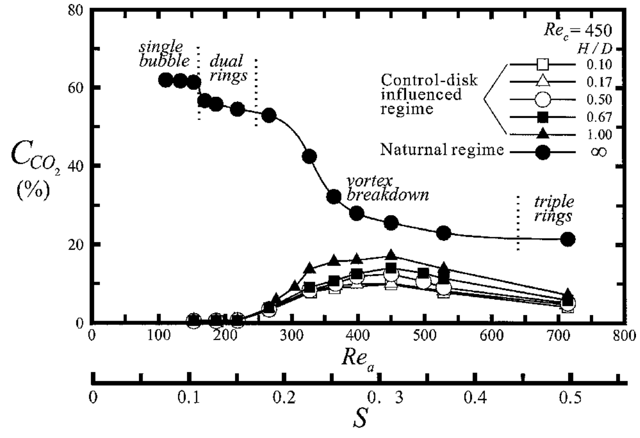

Fig. 11a Carbon-dioxide concentrations of flows in various characteristic regimes.

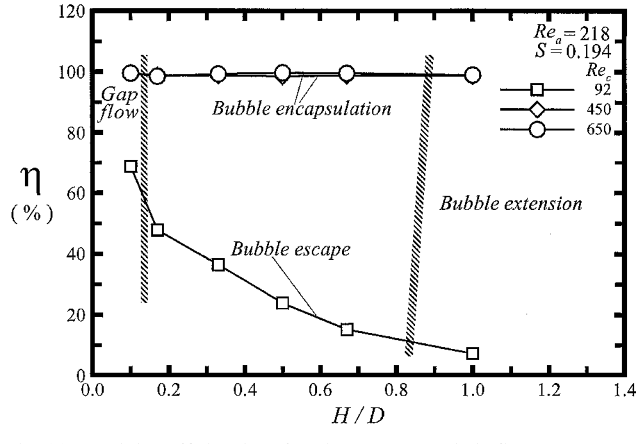

Fig. 11b Mixing efficiencies of various characteristic flows. Measured at $r = 0$ and $x/D = 1.33$.

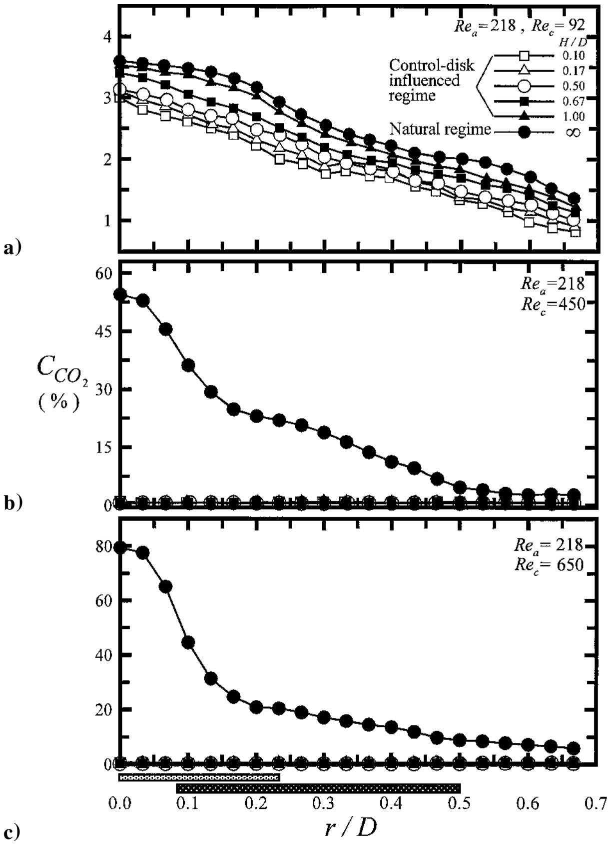

Fig. 12 Radial distributions of carbon-dioxide concentrations of flows in various characteristic regimes.

natural flow measured at $(r/D, x/D) = (0, 1.33)$. A large value of η indicates a high efficiency of mixing compared with the flows in the natural regime. Influences of H/D on the mixing efficiency η at various Re_c are shown in Fig. 11b. At large $Re_c = 4.5 \times 10^2$ and 6.5×10^2, η can attain almost 100% for all H/D. At $Re_c = 9.2 \times 10$, however, η decreases with the increase of H/D and is much smaller than 100%. Operating this type of apparatus in the bubble encapsulation and gap flow regimes can obtain a high mixing efficiency. At low central jet Reynolds numbers the distance between the control disk and the blockage disk has to be decreased in order to obtain large mixing efficiency.

Figure 12 shows the typical radial CO_2 distributions of the flows in the natural and control-disk-influenced regimes at various H/D. The gases are sampled across the level $x/D = 1.33$. At a low central jet Reynolds number $Re_c = 9.2 \times 10$, as shown in Fig. 12a, the spatial gradients of the radial CO_2 concentration profiles for natural flow and the disk-controlled flows do not display significant differences. However, at large central jet Reynolds numbers $Re_c = 4.5 \times 10^2$ and 6.5×10^2, as shown in Figs. 12b and 12c, respectively, the spatial gradients of the radial CO_2 concentration profiles of the disk-controlled flows become almost negligible when compared with those of the flows in natural regime. The high dispersion efficiency is attained because of the drastic increase in lateral and axial turbulent diffusions, which is induced through the direction change of the mean flow momentum flux from the axial to the lateral direction.

Conclusions

A flow-control method by using an above-exit disk to circumvent the injection-through problem of the high-speed central jet in the swirling vortical wakes is studied. The following conclusions are drawn from the results and discussion:

1) Depending on the distance between the control and the blockage disks and the central jet Reynolds number, the flow structures of the swirling vortical wakes can be modulated. The flowfields could be grouped as natural state, bubble extension, bubble escape, bubble encapsulation, and gap flow. The extension of the bubble occurs when the up-shear effect of the deflected central jet stretches axially of the swirling vortical bubble. The escape of the outer vortex ring occurs when the deflected central jet is not strong enough and turns upward near the disk rim. The encapsulation of the dual-ring flow structure is caused by the blockage effect induced by large deflected central jet momentum.

2) In the bubble encapsulation and gap flow regimes a large amount of the axial momentum of the mean flow is transferred to the lateral one in the downstream area of the control disk as a result of the deflection of the central jet. This transformation of momentum from axial to lateral direction induces a drastic increase of the lateral turbulent fluctuations in the whole wake region and a moderate increase of the axial fluctuations in the wake region excluding the central core area.

3) An increased mass diffusion between the central jet fluid and the annular swirling flow was induced by the dramatic increase in the turbulent fluctuations and lateral convective currents. This modulation of the flow characteristics leads to a high mixing capability.

Acknowledgment

This research was supported by the National Science Council of the Republic of China under Grant NSC 90-2212-E-011-064.

References

[1] Gupta, A. K., Lilley, D. G., and Syred, N., *Swirl Flows*, Abacus, Cambridge, MA, 1984, pp. 13–117.

[2] Rose, W. G., "A Swirling Round Turbulent Jet—Mean-Flow Measurements," *Journal of Applied Mechanics*, Vol. 29, Dec. 1962, pp. 615–625.

[3] Chigier, N. A., and Beer, J. M., "Velocity and Static Pressure Distributions in Swirling Air Jets Issuing from Annular and Divergent Nozzles," *Journal of Basic Engineering*, Vol. 86, Dec. 1964, pp. 788–798.

[4] Escudier, M. P., and Keller, J. J., "Recirculation in Swirling Flow: A Manifestation of Vortex Breakdown," *AIAA Journal*, Vol. 23, No. 1, 1985, pp. 111–116.

[5] Leibovich, S., "Vortex Stability and Breakdown: Survey and Extension,"*AIAA Journal*, Vol. 22, No. 9, 1983, pp. 1192–1206.

[6] Sloan, D. G., Smith, P. J., and Smoot, L. D., "Modeling of Swirl in Turbulent Flow Systems," *Progress in Energy and Combustion Science*, Vol. 12, 1986, pp. 163–250.

[7] Sheen, H. J., Chen, W. J., and Jeng, S. Y., "Recirculation Zones of Unconfined and Confined Annular Swirling Jets," *AIAA Journal*, Vol. 34, No. 3, 1996, pp. 572–579.

[8] Huang, R. F., and Tsai, F. C., "Observations of Swirling Flows Behind Circular Disks," *AIAA Journal*, Vol. 39, No. 6, 2001, pp. 1106–1112.

[9] Tsai, F. C., "Flow Structure and Mixing Characteristics of Swirling Wakes," Ph.D. Dissertation, Dept. of Mechanical Engineering, National Taiwan Univ. of Science and Technology, Taipei, Taiwan, ROC, 2001, pp. 26–28.

[10] Chigier, N. A., and Chervinsky, A., "Experimental Investigation of Swirling Vortex Motions in Jets," *Journal of Applied Mechanics*, Vol. 89, June 1967, pp. 443–451.

[11] Huang, R. F., and Tsai, F. C., "Flow Field Characteristics of Swirling Double Concentric Jets," *Experimental Thermal and Fluid Science*, Vol. 25, No. 1, 2001, pp. 151–161.

[12] Mueller, T. J., "Flow Visualization by Direct Injection," *Fluid Mechanics Measurements*, 2nd ed., edited by R. J. Goldstein, Taylor and Francis, Washington, DC, pp. 367–450.

[13] Flagan, R. C., and Seinfeld, J. H., *Fundamentals of Air Pollution Engineering*, Prentice–Hall, Upper Saddle River, NJ, 1988, pp. 295–307.

[14] Mei, R., "Velocity Fidelity of Flow Tracer Particles," *Experiments in Fluids*, Vol. 22, No. 1, 1996, pp. 1–13.

[15] Huang, R. F., and Lin, C. L., "Flow Characteristics and Shear-Layer Vortex Shedding of Double Concentric Jets," *AIAA Journal*, Vol. 35, No. 5, 1997, pp. 887–892.

[16] Perry, A. E., and Fairlie, B. D., "Critical Points in Flow Patterns," *Advances in Geophysics B*, Vol. 18, 1974, pp. 299–315.

[17] Chong, M. S., and Perry, A. E., "A General Classification of Three-Dimensional Flow Fields," *Physics of Fluids A*, Vol. 2, No. 5, 1990, pp. 765–777.

[18] Lighthill, M. J., *Laminar Boundary Layers*, Oxford Univ. Press, Oxford, 1963, pp. 48–88.

[19] Perry, A. E., and Steiner, T. R., "Large-Scale Vortex Structures in Turbulent Wakes Behind Bluff Bodies. Part 1. Vortex Formation," *Journal of Fluid Mechanics*, Vol. 174, Pt. 1, 1987, pp. 233–270.

[20] Hunt, J. C. R., Abell, C. J., Peterka, J. A., and Woo, H., "Kinematical Studies of the Flows Around Free or Surface-Mounted Obstacles; Applying Topology to Flow Visualization," *Journal of Fluid Mechanics*, Vol. 86, Pt. 1, 1978, pp. 179–200.

J. P. Gore
Associate Editor